Modeling and simulation of droplet evaporation using a modified Cahn–Hilliard equation

Hyun Geun Lee[a], Junxiang Yang[b], Sangkwon Kim[b], Junseok Kim[b,*]

[a] Department of Mathematics, Kwangwoon University, Seoul 01897, Republic of Korea
[b] Department of Mathematics, Korea University, Seoul 02841, Republic of Korea

ARTICLE INFO

ABSTRACT

In this paper, we propose a mathematical model, its numerical scheme, and some computational experiments for droplet evaporation. In order to model the evaporation, a classical Cahn–Hilliard equation with an interfacial evaporation mass flux term is proposed. An unconditionally gradient stable scheme is used to discretize the governing equation, and the multigrid method is applied to solve the resulting system. The proposed model is first validated via a proper interfacial parameter ϵ, and then, the effect of evaporation rate and effect of contact angle on volume and surface area changes are investigated. The numerical results indicate that the dynamics of evaporation are dependent on the contact angle on a solid substrate.

1. Introduction

The evaporation phenomenon of a droplet on a solid substrate is fundamental to the coffee-ring effect [1] and includes applications such as nanochromatography for disease diagnostics [2]. Numerous experimental [3–7] and numerical [8–11] studies were performed to examine the evaporation phenomenon. The authors of [12] investigated the effect of support fibers on the process of droplet evaporation. An extant study [13] presented a level-set approach to directly simulate the particle motion in droplet evaporation. The evaporation effect was modeled by applying the coupled vapor fraction and temperature conditions to the interface. A previous study [14] numerically investigated 3D particle motion in the evaporation process of a liquid film. The level-set based method was adopted to track the liquid–solid and gas–liquid interfaces. The effects of evaporation, solid particles, and contact line were considered in the proposed method.

Among the many existing simulation models for evaporation phenomena, phase-field models attracted considerable attention. In [15], the Allen–Cahn (AC) type model with a contact angle was developed to investigate droplet evaporation for different shapes of the gas-liquid interface. In the model, the evaporation energy density is given as $f_{evap}(\phi) = p(c_s - c_p)\phi^2(3 - 2\phi)$, where p denotes the ambient pressure, c_s and c_p denote the saturated concentration and current concentration of liquid in the gas, respectively.

The main purpose of this study is to formulate a modified Cahn–Hilliard (CH) model to simulate droplet evaporation. The CH equation [16,17] has been extensively used in literature to model evolving interface problems. For physical, mathematical, and numerical derivations of the CH equation, interested readers can refer to a review paper [18]. Although the AC type

---

* Corresponding author.
E-mail address: cfdkim@korea.ac.kr (J. Kim).
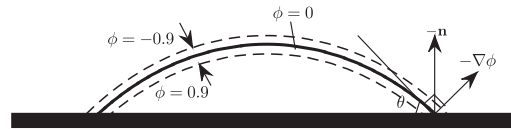*URL:* http://www.math.korea.ac.kr/pl2X-sim-cfdkim (J. Kim)

Fig. 1. Schematic illustration of the contact angle.

model is simple, i.e., the second-order partial differential equation (PDE), the total mass is not conservative in the absence of evaporation. The proposed model corresponds to the fourth-order PDE and is more difficult to solve than the AC equation. However, it is conservative in the absence of evaporation. Furthermore, efficient numerical solvers are available.

The remainder of this paper are organized as follows. In Section 2, the proposed mathematical model for droplet evaporation is presented. In Section 3, the description of the numerical algorithm is given. The numerical results are given in Section 4, and conclusions are discussed in Section 5.

2. Proposed mathematical model for droplet evaporation

As the case of a tumor growth [19–21] model, we propose the following governing equation by adding an evaporation term to the CH equation with a contact angle boundary condition [22] to model the evaporation of a droplet with a contact angle on a solid substrate as follows:

$$\frac{\partial \phi(\mathbf{x},t)}{\partial t} = \frac{1}{Pe}\Delta \mu(\mathbf{x},t) - \gamma |\nabla \phi(\mathbf{x},t)|, \quad \mathbf{x} = (x,y,z) \in \Omega, \ 0 < t \leq T, \tag{1}$$

$$\mu(\mathbf{x},t) = F'(\phi(\mathbf{x},t)) - \epsilon^2 \Delta \phi(\mathbf{x},t), \tag{2}$$

$$\mathbf{n} \cdot \nabla \phi(\mathbf{x},t) = \frac{\sqrt{2F(\phi(\mathbf{x},t))}}{\epsilon}\cos\theta, \quad \mathbf{x} = (x,y,z) \in \partial\Omega, \ 0 < t \leq T, \tag{3}$$

$$\mathbf{n} \cdot \nabla \mu(\mathbf{x},t) = 0, \tag{4}$$

where $\phi(\mathbf{x},t)$ denotes an order parameter such as the mass fraction difference of the components ($\phi = 1$ represents the pure liquid and $\phi = -1$ describes the pure gas regions), $\mu(\mathbf{x},t)$ denotes the chemical potential, Pe denotes a constant parameter related to the dynamics of evolution, and γ is an evaporation constant. $\Omega \subset \mathbb{R}^3$ denotes the computational domain, and $\mathbf{n}$ denotes a unit vector that is normal to the domain boundary $\partial\Omega$. Specifically, $F(\phi) = 0.25(\phi^2 - 1)^2$ is a bulk free energy density with minima in the bulks of the liquid and gas phases, ϵ denotes a constant related to the transition layer, and θ denotes a contact angle.

Eqs. (1) –(4) without the evaporation term $-\gamma|\nabla\phi(\mathbf{x},t)|$ arise from the following free energy functional:

$$\mathcal{F}(\phi) = \mathcal{E}(\phi) + \mathcal{W}(\phi) = \int_\Omega \left(F(\phi) + \frac{\epsilon^2}{2}|\nabla\phi|^2\right)d\mathbf{x} + \int_{\partial\Omega} G(\phi) \ ds,$$

where $G(\phi) = \epsilon(\phi^3 - 3\phi)\cos\theta/(3\sqrt{2})$ [23] denotes the wall free energy function depending on θ. We briefly derive Eqs. (1)–(4) as follows. Let $\int_\Omega \psi \ d\mathbf{x} = 0$. Subsequently, we obtain

$$\begin{aligned}\frac{d}{d\eta}\mathcal{F}(\phi + \eta\psi)\bigg|_{\eta=0} &= \int_\Omega \left(\psi F'(\phi) + \epsilon^2 \nabla\psi \cdot \nabla\phi\right)d\mathbf{x} + \int_{\partial\Omega} \psi G'(\phi)ds \\ &= \int_\Omega \left(F'(\phi) - \epsilon^2\Delta\phi\right)\psi \, d\mathbf{x} + \int_{\partial\Omega}\left(\epsilon^2 \mathbf{n}\cdot\nabla\phi + G'(\phi)\right)\psi \, ds \\ &= \int_\Omega \left(F'(\phi) - \epsilon^2\Delta\phi\right)\psi \, d\mathbf{x}, \end{aligned} \tag{5}$$

where the natural boundary condition is applied as follows:

$$\mathbf{n}\cdot\nabla\phi = -\frac{G'(\phi)}{\epsilon^2}. \tag{6}$$

Subsequently, from Eq. (5), the variational derivative is given as $\mu = F'(\phi) - \epsilon^2\Delta\phi$. The definition of flux is $\mathcal{J} := -M\nabla\mu$, where M denotes a positive mobility. By the mass conservation condition, we obtain $\phi_t = -\nabla \cdot \mathcal{J}$, which leads to the CH Eqs. (1) and (2).

From Fig. 1, we obtain

$$\mathbf{n}\cdot\nabla\phi = |\mathbf{n}||\nabla\phi|\cos\theta = |\nabla\phi|\cos\theta.$$
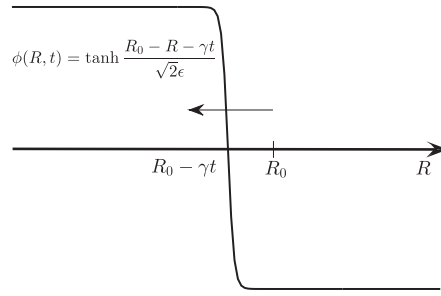
Fig. 2. Concentration profile.

An equilibrium solution of Eqs. (1) and (2) without the evaporation term satisfies the following relation:

$$F(\phi) = 0.5\epsilon^2 |\nabla\phi|^2.$$

Therefore, $|\nabla\phi| = \sqrt{2F(\phi(\mathbf{x},t))}/\epsilon = (\phi^2 - 1)/(\sqrt{2}\epsilon)$ and Eq. (6) becomes Eq. (3).

Next, we derive the evaporation term. For simplicity of exposition because there is a simple closed-form solution for a spherical drop, we consider the case of a spherical drop of radius R. S and V denote the surface area and volume, respectively. Subsequently, we assume that the evaporation rate dV/dt is proportional to S. That is,

$$\frac{dV}{dt} = -\gamma S, \tag{7}$$

where γ denotes the evaporation constant. Eq. (7) becomes $dR/dt = -\gamma$, and its solution is $R(t) = R_0 - \gamma t$, where R_0 denotes the initial drop radius. We consider a profile (see Fig. 2),

$$\phi(R, t) = \tanh\frac{R_0 - R - \gamma t}{\sqrt{2}\epsilon}. \tag{8}$$

Differentiating Eq. (8) yields

$$\frac{\partial\phi(R,t)}{\partial t} = -\frac{\gamma}{\sqrt{2}\epsilon}\text{sech}^2\frac{R_0 - R - \gamma t}{\sqrt{2}\epsilon} = -\frac{\gamma}{\sqrt{2}\epsilon}\left(1 - \tanh^2\frac{R_0 - R - \gamma t}{\sqrt{2}\epsilon}\right)$$

$$= -\frac{\gamma}{\sqrt{2}\epsilon}\left(1 - \phi^2(R,t)\right) = -\gamma\frac{\sqrt{2F(\phi(R,t))}}{\epsilon} = -\gamma|\nabla\phi(R,t)|,$$

where we used Eq. (7). In the standard coordinate, we obtain the following equation:

$$\frac{\partial\phi(\mathbf{x},t)}{\partial t} = -\gamma|\nabla\phi(\mathbf{x},t)|. \tag{9}$$

Finally, adding the evaporation term in Eq. (9) to the CH equation with the contact angle boundary condition yields Eqs. (1)–(4). We note that Eqs. (1)–(4) can be derived by considering the sum of two types of gradient flows, as shown in image inpainting using the CH equation [24].

The advantages of the proposed model include its simplicity and practical applicability for modeling more complex physical phenomena such as the coffee-ring effect.

3. Numerical implementation algorithm

The numerical algorithm is introduced in this section. We first present the finite difference scheme for the three-dimensional CH equation on $\Omega = (0, L_x) \times (0, L_y) \times (0, L_z)$. Let N_x, N_y, and N_z denote the mesh numbers along x-, y-, and z-directions, $h = L_x/N_x$ denote the uniform spatial step, $\Omega_h = \{(x_i, y_j, z_k) : x_i = (i - 0.5)h, y_j = (j - 0.5)h, z_k = (k - 0.5)h\}$, where $1 \le i \le N_x, 1 \le j \le N_y, 1 \le k \le N_z$, and ϕ_{ijk}^n denote an approximation of $\phi(x_i, y_j, z_k, n\Delta t)$, where Δt denotes the time step. $Pe = 1$ is used for the purpose of simplicity. Subsequently, the discretization of Eqs. (1) and (2) are expressed as

$$\frac{\phi_{ijk}^{n+1} - \phi_{ijk}^n}{\Delta t} = \frac{1}{Pe}\Delta_d\mu_{ijk}^{n+1} - \gamma|\nabla_d\phi_{ijk}^n|, \tag{10}$$

$$\mu_{ijk}^{n+1} = F'(\phi_{ijk}^{n+1}) + \phi_{ijk}^{n+1} - \phi_{ijk}^n - \epsilon^2\Delta_d\phi_{ijk}^{n+1}, \tag{11}$$

where $\nabla_d\phi_{ijk}^n = (1/2h)\left(\phi_{i+1,jk}^n - \phi_{i-1,jk}^n, \phi_{i,j+1,k}^n - \phi_{i,j-1,k}^n, \phi_{ij,k+1}^n - \phi_{ij,k-1}^n\right)$ and $\Delta_d\mu_{ijk}^{n+1} = (\mu_{i-1,jk}^{n+1} + \mu_{i+1,jk}^{n+1} + \mu_{i,j-1,k}^{n+1} + \mu_{i,j+1,k}^{n+1} + \mu_{ij,k-1}^{n+1} + \mu_{ij,k+1}^{n+1} - 6\mu_{ijk}^{n+1})/h^2$. For μ, we apply homogeneous Neumann boundary conditions in the x-, y-, and
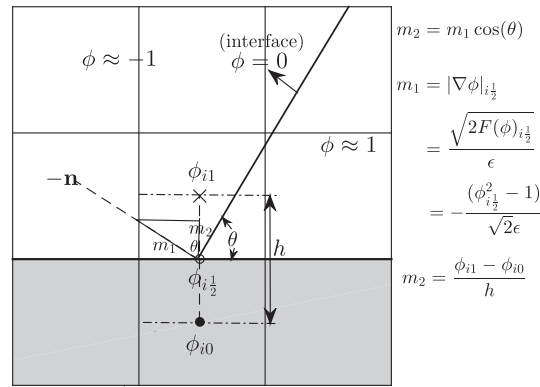
Fig. 3. Schematic illustration of the contact angle boundary condition in two-dimensional space.

z-directions:

$$\mu_{0jk}^{n+1} = \mu_{1jk}^{n+1}, \ \mu_{N_x+1,jk}^{n+1} = \mu_{N_xjk}^{n+1} \quad \text{for } 1 \le j \le N_y, 1 \le k \le N_z,$$

$$\mu_{i0k}^{n+1} = \mu_{i1k}^{n+1}, \ \mu_{i,N_y+1,k}^{n+1} = \mu_{iN_yk}^{n+1} \quad \text{for } 1 \le i \le N_x, 1 \le k \le N_z,$$

$$\mu_{ij0}^{n+1} = \mu_{ij1}^{n+1}, \ \mu_{ij,N_z+1}^{n+1} = \mu_{ijN_z}^{n+1} \quad \text{for } 1 \le i \le N_x, 1 \le j \le N_y.$$

Boundary conditions for ϕ are the same as μ except at $z = 0$:

$$\phi_{0jk}^{n+1} = \phi_{1jk}^{n+1}, \ \phi_{N_x+1,jk}^{n+1} = \phi_{N_x,jk}^{n+1} \quad \text{for } 1 \le j \le N_y, 1 \le k \le N_z,$$

$$\phi_{i0k}^{n+1} = \phi_{i1k}^{n+1}, \ \phi_{i,N_y+1,k}^{n+1} = \phi_{i,N_y,k}^{n+1} \quad \text{for } 1 \le i \le N_x, 1 \le k \le N_z,$$

$$\phi_{ij,N_z+1}^{n+1} = \phi_{ijN_z}^{n+1} \quad \text{for } 1 \le i \le N_x, 1 \le j \le N_y.$$

On the substrate (i.e., $z = 0$), we note that $\mathbf{n} = (0, 0, -1)$, then Eq. (3) is expressed as

$$-\phi_z = \frac{1 - \phi^2}{\sqrt{2}\epsilon} \cos\theta. \tag{12}$$

If we discretize Eq. (12), then we have the discrete form:

$$-\phi_r = -\frac{\phi_{ij1} - \phi_{ij0}}{h} = -\frac{(\phi_{ij\frac{1}{2}}^2 - 1)\cos\theta}{\sqrt{2}\epsilon}. \tag{13}$$

Then, the contact angle boundary condition in Eq. (13) is expressed as

$$\phi_{ij0} = \phi_{ij1} - \frac{h(\phi_{ij\frac{1}{2}}^2 - 1)\cos\theta}{\sqrt{2}\epsilon}, \tag{14}$$

where $\phi_{ij\frac{1}{2}} = (3\phi_{ij1} - \phi_{ij2})/2$, which corresponds to a linear interpolation. The values at $k = 1$ and $k = 2$ are used to calculate the unknown value at $k = 1/2$. A schematic illustration of the contact angle boundary condition in two-dimensional view is shown in Fig. 3.

We note that the central difference discretization is used for the gradient term and standard seven-point discretization is used for the Laplacian operator; therefore, the convergence rate in space is second-order. For the time discretization, an unconditionally stable scheme is used for the CH model, and the evaporation term is treated explicitly, thus the convergence rate in time is first-order. Specifically, the multigrid method with V-cycle is applied to solve Eqs. (10) and (11), and thus the computational complexity is $\mathcal{O}(N \log N)$, where N denotes the number of mesh grid points. More details on the numerical method are given in [25].

4. Numerical results

In the numerical tests, the homogeneous Neumann boundary condition is applied at the boundaries in x-direction, y-direction, and $z = L_z$. At $z = 0$, we give a contact angle boundary condition. We use $Pe = 1$ for the purposed of simplicity in all numerical tests.
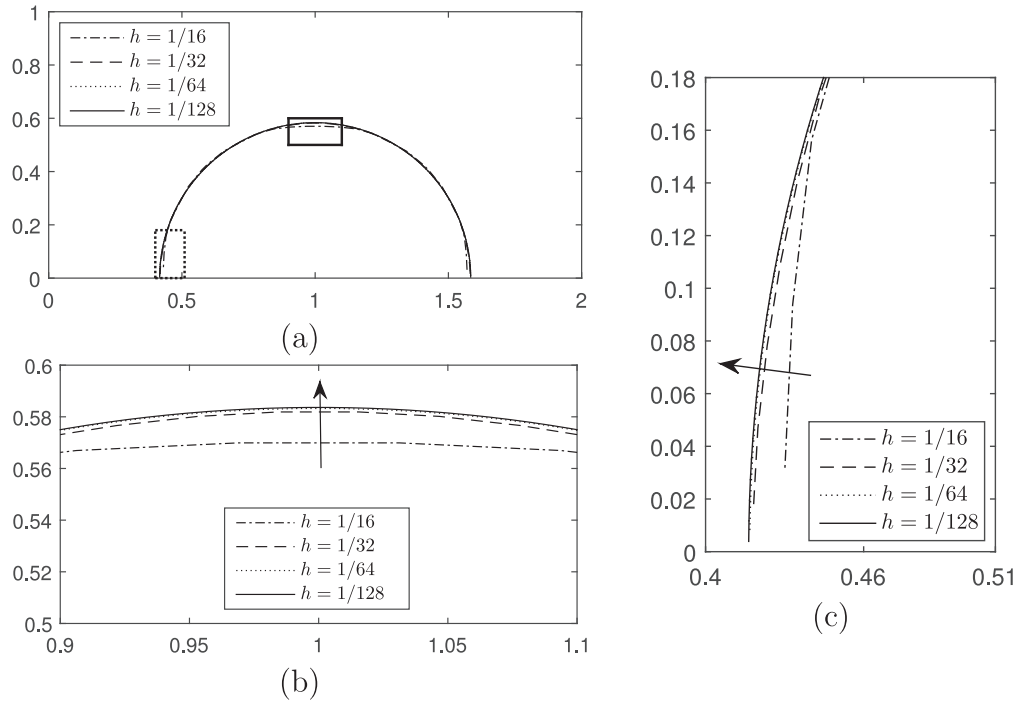
Fig. 4. (a) Interface profiles at numerical equilibrium state. (b) Locally enlarged views of the solid box region (c) and dotted box region. Arrow denotes the convergence direction.

4.1. Mesh convergence

First, we investigate the convergence of the CH equation with respect to the mesh size h. Specifically, the evaporation rate is set as $\gamma = 0$ and we use zero Neumann boundary condition on the bottom boundary. We use the following four different mesh sizes: $h = 1/16$, $1/32$, $1/64$, and $1/128$ in the domain $\Omega = (0,2) \times (0,2) \times (0,1)$. The other numerical parameters are $\Delta t = 1/128$ and $\epsilon = 0.045$. We define the following initial condition

$$\phi(x,y,z,0) = \begin{cases} 1 & \text{if } 0.5 \le x \le 1.5, \ 0.5 \le y \le 1.5, \ z \le 0.5, \\ -1 & \text{otherwise.} \end{cases}$$

The computation stops when the numerical equilibrium state is reached (i.e., $\|\phi^{n+1} - \phi^n\|_2 \le 10^{-5}$, where ϕ^{n+1} and ϕ^n denote the results at $(n+1) - th$ and $n - th$ time step, respectively). The numerical equilibrium solutions are shown in Fig. 4(a). Fig. 4(b) and (c) show the locally enlarged views of the solid box and dotted box regions in Fig. 4(a), respectively. We observe that the equilibrium solutions converge with respect to grid size. In order to achieve an accurate computation, we use $h = 1/128$ (i.e., a mesh grid: $256 \times 256 \times 128$) in the following tests.

It is noted that the proposed numerical scheme uses the center difference discretization for the gradient term and standard seven-point discretization for the Laplacian operator; thus, the second-order accuracy will be obtained in space. To numerically demonstrate the convergence order in space, we use the result with $h = 1/128$ as a reference solution because the closed-form solution does not exist. A series of successively finer mesh sizes: $h = 1/16$, $1/32$, and $1/64$ are selected. The error between numerical and reference solutions is defined as follows:

$$\begin{aligned}
e^h = \ &\phi^h_{ijk} - \frac{1}{8}\big(\phi^r_{2^p i-p,2^p j-p,2^p k-p} + \phi^r_{2^p i-p+1,2^p j-p+1,2^p k-p+1} \\
&+ \phi^r_{2^p i-p,2^p j-p+1,2^p k-p+1} + \phi^r_{2^p i-p+1,2^p j-p,2^p k-p+1} + \phi^r_{2^p i-p+1,2^p j-p+1,2^p k-p} \\
&+ \phi^r_{2^p i-p+1,2^p j-p,2^p k-p} + \phi^r_{2^p i-p,2^p j-p+1,2^p k-p} + \phi^r_{2^p i-p,2^p j-p,2^p k-p+1}\big),
\end{aligned}$$

where ϕ^h and ϕ^r denote the numerical and reference solutions, respectively. Specifically, $p = 3$, 2, and 1 denote errors for $h = 1/16$, $1/32$, and $1/64$, respectively. The rate of convergence is defined as the ratio of successive errors: $\log_2\left(\|e^h\|_2/\|e^{\frac{h}{2}}\|_2\right)$. Specifically, $\|e\|_2$ is a discrete l_2-norm and is defined as $\|e\|_2 = \sqrt{\sum_{i=1}^{N_x}\sum_{j=1}^{N_y}\sum_{k=1}^{N_z} e_{ijk}^2/(N_x N_y N_z)}$. As shown in Table 1, second-order accuracy in space is obtained.

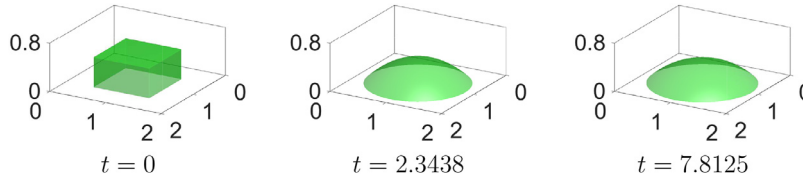**Table 1**
Errors and convergence rates with different spatial steps.

Mesh size	$h = 1/16$		$h = 1/32$		$h = 1/64$
Error	0.0204		0.0049		0.0011
Rate		2.0577		2.1553	

Table 2
Convergence results of mesh refinement for $\theta = 45°$ and $135°$.

Mesh grids	$64 \times 64 \times 32$	$128 \times 128 \times 64$	$256 \times 256 \times 128$	Theoretical angle
Numerical angle	$39.2529°$	$45.7280°$	$44.8040°$	$45°$
	$137.7893°$	$136.0309°$	$135.2348°$	$135°$

Fig. 5. Temporal evolution of droplet with $\theta = 45°$.
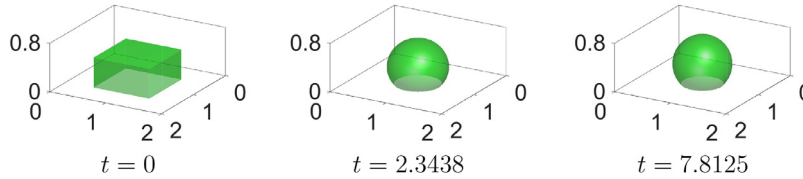
Fig. 6. Temporal evolution of droplet with $\theta = 135°$.

4.2. Equilibrium contact angles

Next, we consider an equilibrium state of a droplet contacting a solid substrate with a prescribed contact angle θ, $\epsilon = 0.045$, $\gamma = 0$, and $\Delta t = 1/128$. The initial condition on $\Omega = (0, 2) \times (0, 2) \times (0, 1)$ is

$$\phi(x, y, z, 0) = \begin{cases} 1 & \text{if } 0.5 \le x \le 1.5, \ 0.5 \le y \le 1.5, \ z \le 0.5, \\ -1 & \text{otherwise.} \end{cases}$$

Figs. 5 and 6 show the temporal evolutions of the droplet for two different θ corresponding to $\theta = 45°$ and $\theta = 135°$.

The convergence results of mesh refinement for different θ are listed in Table 2. To find a numerical contact angle, we use the following procedure. Given three points (x_1, z_1), (x_2, z_2), and (x_3, z_3) on the '$y = 1$'-interface, we calculate the center and the radius of the circle which passes through the three points. We compute the center points x_c and z_c from

$$(x_1 - x_c)^2 + (z_1 - z_c)^2 = (x_2 - x_c)^2 + (z_2 - z_c)^2,$$
$$(x_2 - x_c)^2 + (z_2 - z_c)^2 = (x_3 - x_c)^2 + (z_3 - z_c)^2,$$

and calculate the radius $r = \sqrt{(x_i - x_c)^2 + (z_i - z_c)^2}$. Then the x-intercepts of the circle are $x = x_c \pm \sqrt{r^2 - z_c^2}$ and a derivative at the contact point is

$$\tan \theta = \frac{dz}{dx}\left(x_c + \sqrt{r^2 - z_c^2}, 0\right) = \frac{\sqrt{r^2 - z_c^2}}{z_c}.$$

Finally, we define the numerical contact angle as $\theta = \mod(\tan^{-1}(\sqrt{r^2 - z_c^2}/z_c), \pi)$. As shown in the table, the numerical results converge to theoretical contact angles with finer meshes.

4.3. Dynamics of CH equation without evaporation

We investigate the dynamics of the CH equation without evaporation in three-dimensional space. If the mesh size is not sufficiently small, then the dynamics of interface length minimization of the CH equation does not preserve the enclosed volume obtained by its interface. In the actual physical condition, the droplet vanishes in time due to the effect of evaporation. Therefore, in the numerical simulation, it is necessary to eliminate the interface length minimization effect of the CH equation by using a sufficiently small mesh size.
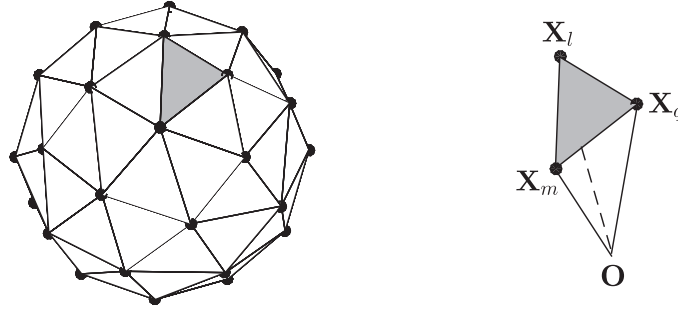
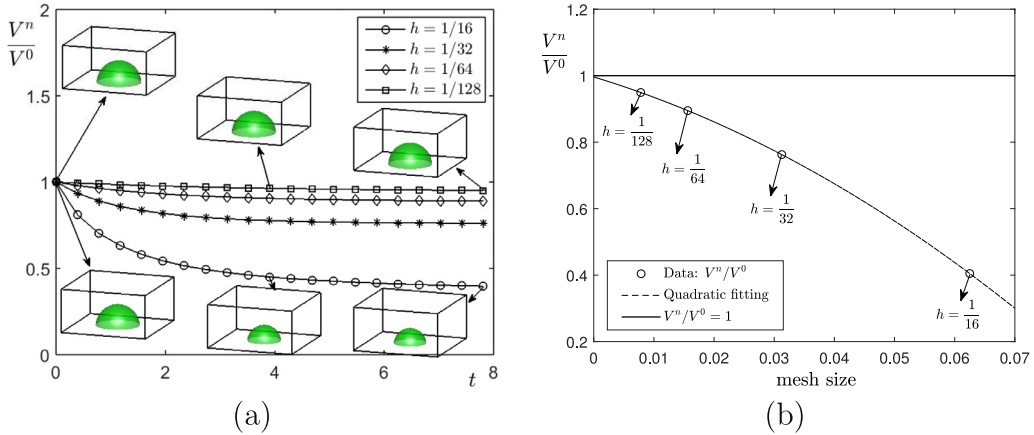**Fig. 7.** Schematic illustration for the polyhedron and a tetrahedron with a reference point **O**.

Fig. 8. (a) Temporal evolutions of discrete volumes of droplet for various mesh sizes h: 1/16, 1/32, 1/64, and 1/128. (b) Quadratic fitting of the values of V^n/V^0 at the final time.

Table 3
Values of V^n/V^0 at the final time.

Mesh size	$h = 1/16$	$h = 1/32$	$h = 1/64$	$h = 1/128$
V^n/V^0	0.4047	0.7626	0.8949	0.9494

Fig. 8 (a) shows the temporal evolutions of discrete volume of droplet without evaporation for various mesh sizes: $h = 1/16$ (circle markers), $h = 1/32$ (star markers), $h = 1/64$ (diamond markers), and 1/128 (square markers). The initial condition in $\Omega = (0, 2) \times (0, 2) \times (0, 1)$ is

$$\phi(x, y, z, 0) = \tanh \frac{0.5 - \sqrt{(x-1)^2 + (y-1)^2 + z^2}}{\sqrt{2}\epsilon}. \tag{15}$$

Specifically, $\Delta t = 1/128$, $\epsilon = 4h/(2\sqrt{2}\tanh^{-1}(0.9))$, and $\gamma = 0$ are used. The discrete volume is defined as

$$V(\mathbf{X}) = \frac{1}{6} \sum_{s=1}^{M_T} [X_q(Y_l Z_m - Y_m Z_l) - Y_q(X_l Z_m - X_m Z_l) + Z_q(X_l Y_m - X_m Y_l)],$$

where M_T denotes the total number of surface triangles $\mathbf{Tri_s} = (\mathbf{X}_l, \mathbf{X}_m, \mathbf{X}_q)$ with a reference point **O**, and each $\mathbf{X}_i$ means (X_i, Y_i, Z_i) [26]. The schematic illustration is shown in Fig. 7. The embedded small figures denote the corresponding evolution states for $h = 1/16$ and $h = 1/128$. It is observed that a sufficiently small mesh size can eliminate the dynamics of interface length minimization of the CH equation. For accurate simulation, we use $h = 1/128$ in the following tests.

Fig. 8 (b) shows the values of V^n/V^0 at the final time with quadratic fitting. The result indicates that V^n/V^0 converges to 1 when h goes to zero. Table 3 shows the values of V^n/V^0 with respect to different step sizes.

4.4. Stability test

In this work, a well-known unconditionally stable scheme is used to solve the classical CH model, and the evaporation term is treated explicitly as a source term. To numerically demonstrate the stability of the numerical method, we select a
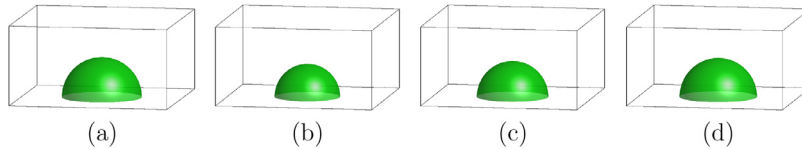
Fig. 9. Numerical stability test: (a) Initial, (b) $\Delta t = h$, (c) $\Delta t = 10$ h, and (d) $\Delta t = 100$ h.
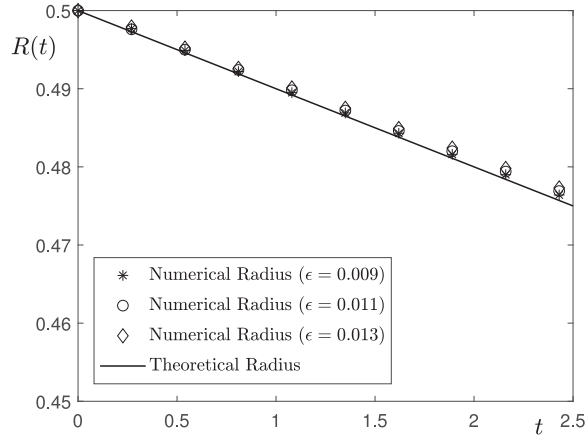
Fig. 10. Temporal evolutions of theoretical (thick solid line) and numerical radii for different values of ϵ: 0.009 (star), 0.011 (open circle), and 0.013 (diamond).

series of increasing time steps: $\Delta t = h$, 10 h, and 100 h to simulate the droplet evaporation with an evaporation constant $\gamma = 0.01$. The initial condition is given by Eq. (15). Fig. 9 shows the results with different time steps at $t = 0.7813$ and we observed that the proposed scheme is stable with large time steps. However, to obtain accurate results, a relatively small time step $\Delta t = h$ is used in the following tests.

4.5. Effect of ϵ

In order to confirm a proper ϵ in evaporation simulation, we compare the temporal evolution of numerical radius for various ϵ values ($\epsilon = 0.009$, 0.011, and 0.013) with the theoretical radius: $R(t) = R_0 - \gamma t$. We consider the simulation parameters: $\gamma = 0.01$, $R_0 = 0.6$, $h = 1/128$, $\Delta t = 1/128$, and $\theta = 90°$, and the initial state

$$\phi(x, y, z, 0) = \tanh \frac{0.5 - \sqrt{(x-1)^2 + (y-1)^2 + z^2}}{\sqrt{2}\epsilon}$$

on $\Omega = (0, 2) \times (0, 2) \times (0, 1)$. In Fig. 10, the solid line denotes the theoretical radius; and the star, open circle, and diamond markers denote the numerical radii for different ϵ values: 0.009, 0.011, and 0.013, respectively. As shown in the figure, the numerical results with different values of ϵ exhibit similar evolutions and are consistent with the theoretical result. For the purpose of convenience, we select $\epsilon = 0.011$ and $\Omega = (0, 2) \times (0, 2) \times (0, 1)$ in the following tests.

4.6. Effect of γ

The evaporation rate γ in Eq. (1) affects the dynamics of the proposed model. To investigate the effect of γ on the evaporation, we consider $\gamma = 0.01$, 0.001, and 0.0001 with $h = 1/128$ and $\Delta t = h$. If we consider a droplet with an initial radius of 0.5 and a contact angle of 90° on the substrate, then the initial volume is $\pi/12$. We fix the initial volume to be $V^0 = \pi/12$ in this test. Then, the theoretical radius R is expressed as a function of θ: $R(\theta) = 0.5\big(2/(\cos^3 \theta - 3\cos \theta + 2)\big)^{\frac{1}{3}}$, and the surface area is calculated by $2\pi R(\theta)(R(\theta) - \hat{R}(\theta))$, where $\hat{R}(\theta) = R(\theta)\cos \theta$. The initial condition is expressed in the following form for any contact angle:

$$\phi(x, y, z, 0) = \tanh \frac{R(\theta) - \sqrt{(x-1)^2 + (y-1)^2 + (z + \hat{R}(\theta))^2}}{\sqrt{2}\epsilon}. \tag{16}$$

In this part, the contact angle $\theta = 30°$ is used because a smaller contact angle causes a larger surface area (see Fig. 13) which is more exposed to evaporation. Thus, we obtain $R(\theta) \approx 1.6938$ and $\hat{R}(\theta) \approx 1.4669$. The first column in Fig. 11 shows snapshots of droplet and the second column denotes plots at $y = 1$ and $z = 0.5$ h for (a) $\gamma = 0.01$, (b) $\gamma = 0.001$, and (c) $\gamma = 0.0001$ at $t = 3.125$.
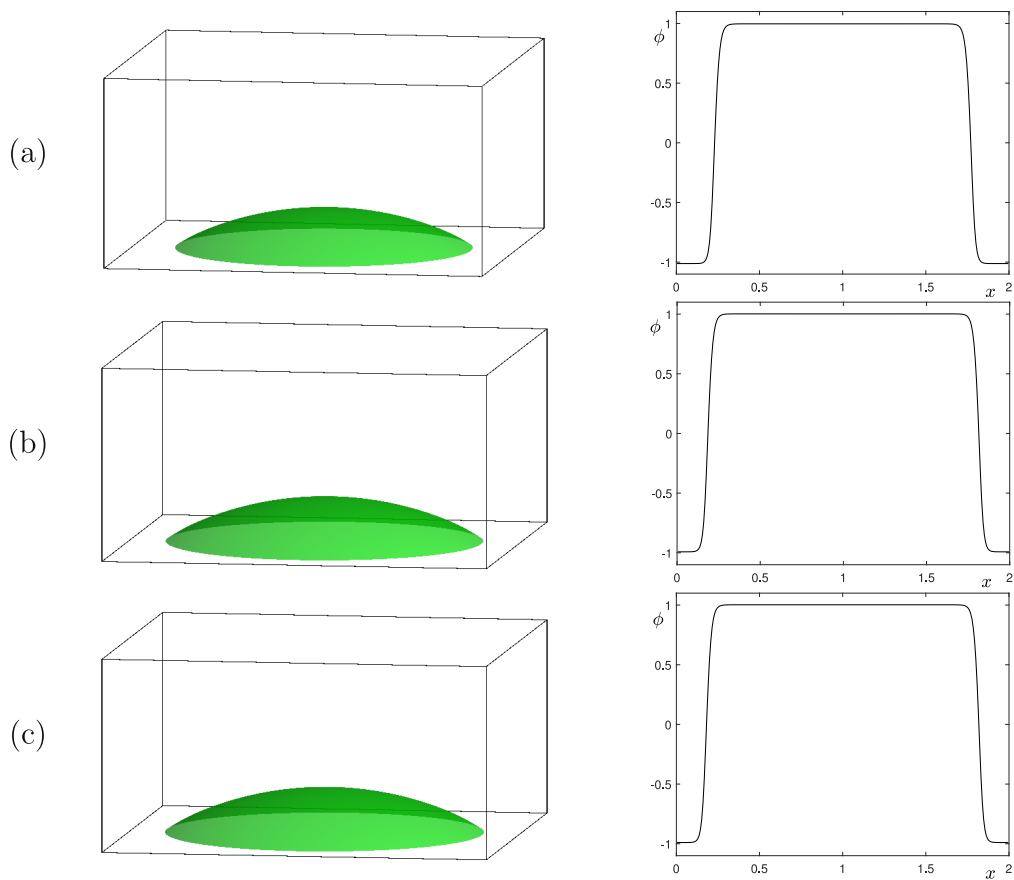
Fig. 11. Snapshots of droplet (left) and plots at $y = 1$ and $z = 0.5h$ (right) for (a) $\gamma = 0.01$, (b) $\gamma = 0.001$, and (c) $\gamma = 0.0001$ at $t = 3.125$.
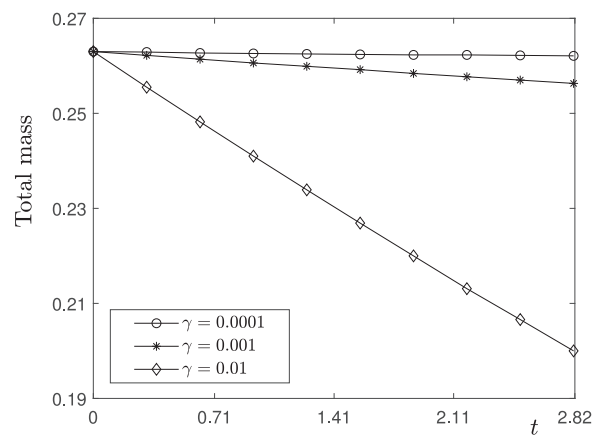

Fig. 12. Temporal evolutions of total mass for different values of γ.

Fig. 12 shows the evolutions of total mass with respect to three different values of γ as follows: 0.01, 0.001, and 0.0001. The definition of total mass is $\sum\limits_{i=1}^{N_x} \sum\limits_{j=1}^{N_y} \sum\limits_{k=1}^{N_z} 4(1 + \phi_{ijk})/(2N_x N_y N_z)$. We can find that the dynamics of evaporation are affected by γ, i.e., a larger value of γ hastens the evaporation process.
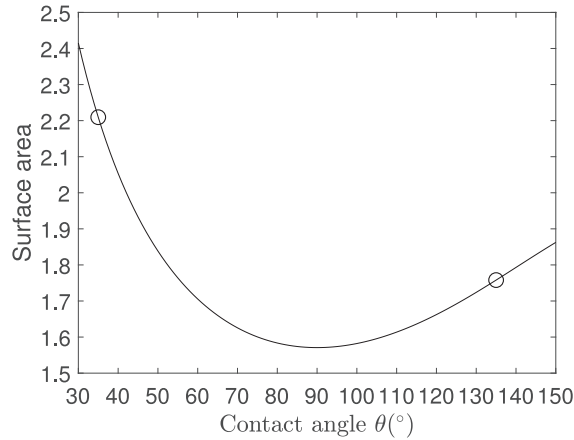
Fig. 13. Surface areas for various contact angles.
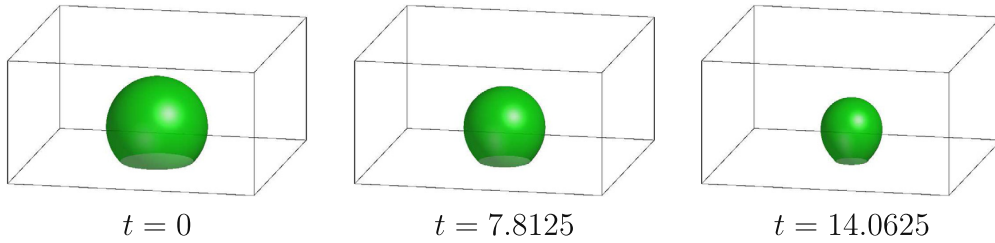
Fig. 14. Temporal evolution of the droplet with the prescribed contact angle $\theta = 135°$.
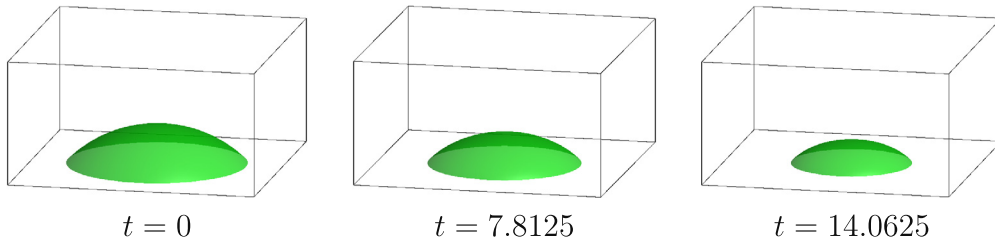
Fig. 15. Temporal evolution of the droplet with the prescribed contact angle $\theta = 45°$.

4.7. Effect of θ on volume change

Herein, we investigate the effect of θ on volume change. The initial volume is set as a fixed value: $V^0 = \pi/12$ for various contact angles. Fig. 13 shows the relationship between surface area and contact angle, and we observe that the surface area decreases with an increase in the angle corresponding to $\theta < 90°$ but increases for $\theta > 90°$. To compare the evaporation dynamics for different surface areas, two specific contact angles $\theta = 45°$ and $135°$ with $\gamma = 0.01$ (see the circle markers in Fig. 13) are used. The general form of the initial state with various θ is

$$\phi(x, y, z, 0) = \tanh \frac{R(\theta) - \sqrt{(x-1)^2 + (y-1)^2 + (z+\hat{R}(\theta))^2}}{\sqrt{2}\epsilon}. \tag{17}$$

Figs. 14 and 15 show the evolutions of the droplet for two different contact angles: $\theta = 135°$ and $\theta = 45°$. Theoretically, the change in total mass satisfies the relation: $dM/dt = -\gamma S$ where M denotes total mass and S denotes surface area, thereby implying that increases in surface area lead to faster decreases in total mass. For a droplet with radius R and contact angle θ, the volume and surface area are represented by $M = \pi R^3 (2 + \cos\theta)(1 - \cos\theta)^2/3$ and $S = 2\pi R^2 (1 - \cos\theta)$, respectively.

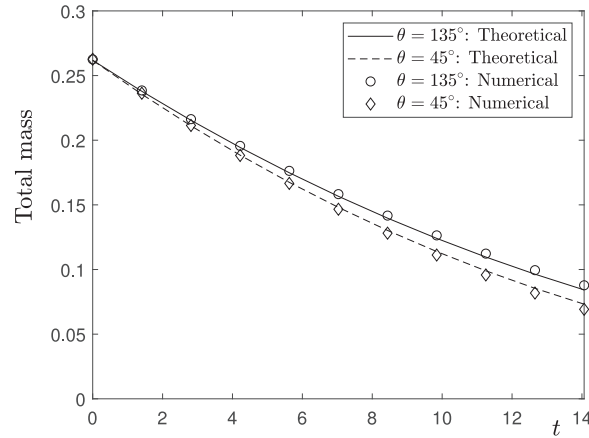**Fig. 16.** Temporal evolutions of total mass for $\theta = 135°$ and $\theta = 45°$.

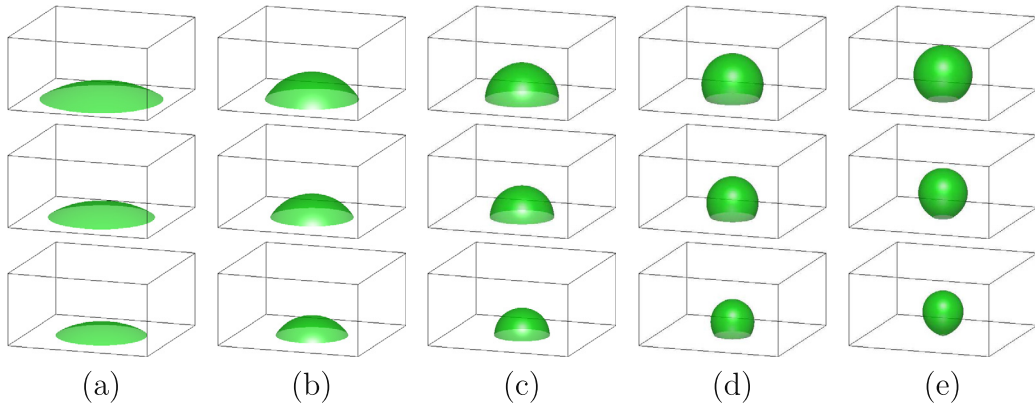**Fig. 17.** Temporal evolutions of droplet evaporation for various contact angles θ: (a) 30°, (b) 60°, (c) 90°, (d) 120°, and (e) 150°. Times from the top to bottom for each column are $t = 0$, 7.8125, and 14.0625.

Hence, we obtain the following relationship:

$$\frac{dR}{dt} = \frac{-2\gamma}{(2 + \cos\theta)(1 - \cos\theta)},\tag{18}$$

and its solution is $R(t) = R_0 - 2\gamma t/((2 + \cos\theta)(1 - \cos\theta))$, where R_0 denotes the initial radius and R denotes the radius at time t. Subsequently, the theoretical mass of a droplet at any computational step can be calculated using the formula of M above. In Fig. 16, we plot the numerical and theoretical values of the mass of the droplet with respect to different contact angles; and we observe that the velocity of mass decrease for 45° (the line with star markers) is greater than that for 135° (the line with circle markers). The numerical result thus exhibits good agreement with theory.

4.8. Effect of θ on surface area change

Finally, we investigate the effect of θ on surface area change with $V^0 = \pi/12$ and various contact angles corresponding to $\theta = 30°$, 60°, 90°, 120°, and 150°. In simulation, we use $h = 1/128$, $\epsilon = 0.011$, $\Delta t = h$, and $\gamma = 0.01$ on $\Omega = (0, 2) \times (0, 2) \times (0, 1)$. The discrete surface area A is defined as

$$A(\mathbf{X}) = \frac{1}{2} \sum_{s=1}^{M_T} |(\mathbf{X}_q - \mathbf{X}_l) \times (\mathbf{X}_m - \mathbf{X}_l)|,$$

where the schematic illustration can be found in Fig. 7. Fig. 17(a)–(d) show the temporal evolutions of droplet evaporation for various contact angles θ corresponding to $30°, 60°, 90°, 120°$, and 150°, respectively. The evolutions of the discrete surface area for various contact angles are shown in Fig. 18, where the different markers denote surface areas at different times. We observe that the distributions of the surface areas for a time are similar.
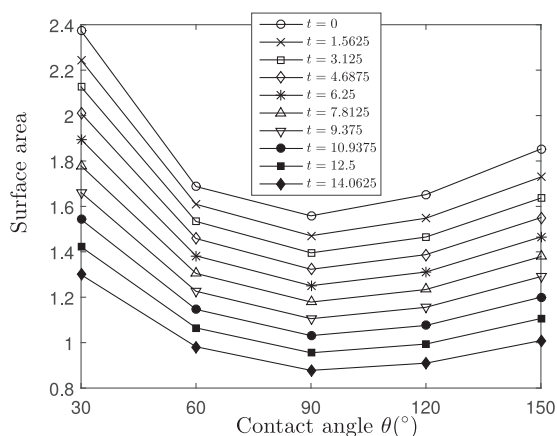
Fig. 18. Temporal evolutions of surface area for various contact angles.

5. Conclusions

We proposed a modified CH model with an interfacial evaporation mass flux to simulate droplet evaporation. To enable fast and efficient computation, the unconditionally gradient stable scheme was used to discretize the governing equation, and the multigrid method was applied to solve the resulting system. The numerical results indicated that the proposed model could simulate droplet evaporation. Additionally, different contact angles lead to different evolutions of total mass and surface area: (a) smaller contact angles cause faster evaporation of the droplet; (b) smaller contact angles cause larger surface areas when $\theta < 90°$, whereas larger contact angles cause larger surface areas when $\theta > 90°$. The surface area of the droplet is least when $\theta = 90°$.

Acknowledgments

References

[1] C. Alexandru, F. Duan, Three-dimensional Monte Carlo model of the coffee-ring effect in evaporating colloidal droplets, Sci. Rep. 4 (2014) 4310, doi:10.1038/srep04310.

[2] T.S. Wong, T.H. Chen, X. Shen, C.M. Ho, Nanochromatography driven by the coffee ring effect, Anal. Chem. 83 (6) (2011) 1871–1873, doi:10.1021/ac102963x.

[3] S.A. Kulinich, M. Farzaneh, Effect of contact angle hysteresis on water droplet evaporation from super-hydrophobic surfaces, Appl. Surf. Sci. 255 (7) (2009) 4056–4060, doi:10.1016/j.apsusc.2008.10.109.

[4] E. Bormashenko, A. Musin, M. Zinigrad, Evaporation of droplets on strongly and weakly pinning surfaces and dynamics of the triple line, Colloids Surf. A 385 (1–3) (2011) 235–240, doi:10.1016/j.colsurfa.2011.06.016.

[5] M.E.R. Shanahan, K. Sefiane, Kinetics of triple line motion during evaporation, Contact Angle Wettability Adhes. 6 (2009) 19–32. Koninklijke Brill, NV, Leiden

[6] M. Amjad, Y. Yang, G. Raza, H. Gao, J. Zhang, L. Zhou, X. Du, D. Wen, Deposition pattern and tracer particle motion of evaporating multi-component sessile droplets, J. Colloid Interface Sci. 506 (2017) 83–92, doi:10.1016/j.jcis.2017.07.025.

[7] C. Diddens, J.G.M. Kuerten, C.W.M. van der Geld, H.M.A. Wijshoff, Modeling the evaporation of sessile multi-component droplets, J. Colloid Interface Sci. 487 (2017) 426–436, doi:10.1016/j.jcis.2016.10.030.

[8] F. Bazdidi-Tehrani, M.S. Abedinejad, Influence of incoming air conditions on fuel spray evaporation in an evaporating chamber, Chem. Eng. Sci. 189 (2) (2018) 233–244, doi:10.1016/j.ces.2018.05.046.

[9] N. Karami, M.H. Rahimian, M. Farhadzadeh, Numerical simulation of droplet evaporation on a hot surface near Leidenfrost regime using multiphase lattice Boltzmann method, Appl. Math. Comput. 312 (2017) 91–108, doi:10.1016/j.amc.2017.05.038.

[10] F. Frank, C. Liu, A. Scanziani, F.O. Alpak, B. Riviere, An energy-based equilibrium contact angle boundary condition on jagged surfaces for phase-field methods, J. Colloid Interface Sci. 523 (2018) 282–291, doi:10.1016/j.jcis.2018.02.075.

[11] H. Jia, Y. Li, G. Feng, K. Li, An efficient two-grid method for the Cahn–Hilliard equation with the concentration-dependent mobility and the logarithmic Flory-Huggins bulk potential, Appl. Math. Comput. (2019) 124548, doi:10.1016/j.amc.2019.06.062.

[12] C. Chauveau, M. Birouk, F. Halter, I. Gökalp, An analysis of the droplet support fiber effect on the evaporation process, Int. J. Heat Mass Transf. 128 (2019) 885–891, doi:10.1016/j.ijheatmasstransfer.2018.09.029.

[13] H. Hwang, G. Son, A level-set method for the direct numerical simulation of particle motion in droplet evaporation, Numer. Heat Tr-B Fund 68 (2015) 479–494, doi:10.1080/10407790.2015.1052309.

[14] H. Hwang, G. Son, Direct numerical simulation of 3D particle motion in an evaporating liquid film, J. Mech. Sci. Technol. 30 (9) (2016) 3929–3934, doi:10.1007/s12206-016-0804-3.

[15] K.M. Schweigler, M.B. Said, S. Seifritz, M. Selzer, B. Nestler, Experimental and numerical investigation of drop evaporation depending on the shape of the liquid/gas interface, Int. J. Heat Mass Transf. 105 (2017) 655–663, doi:10.1016/j.ijheatmasstransfer.2016.10.033.

[16] J.W. Cahn, J.E. Hilliard, Free energy of a nonuniform system. I. Interfacial free energy, J. Chem. Phys. 28 (2) (1958) 258–267, doi:10.1063/1.1744102.
[17] E. Gros, G. Anjos, J. Thome, Moving mesh method for direct numerical simulation of two-phase flow with phase change, Appl. Math. Comput. 339 (2018) 636–650, doi:10.1016/j.amc.2018.07.052.
[18] D. Lee, J.Y. Huh, D. Jeong, J. Shin, A. Yun, J. Kim, Physical, mathematical, and numerical derivations of the Cahn–Hilliard equation, Comput. Mater. Sci. 81 (2014) 216–225, doi:10.1016/j.commatsci.2013.08.027.
[19] S.M. Wise, J.S. Lowengrub, H.B. Frieboes, V. Cristini, Three-dimensional multispecies nonlinear tumor growth–I: model and numerical method, J. Theor. Biol. 253 (2008) 524–543, doi:10.1016/j.jtbi.2008.03.027.
[20] H.B. Frieboes, F. Jin, Y.-L. Chuang, S.M. Wise, J.S. Lowengrub, V. Cristini, Three-dimensional multispecies nonlinear tumor growth–II: tumor invasion and angiogenesis, J. Theor. Biol. 264 (2010) 1254–1278, doi:10.1016/j.jtbi.2010.02.036.
[21] Y. Chen, S.M. Wise, V.B. Shenoy, J.S. Lowengrub, A stable scheme for a nonlinear, multiphase tumor growth model with an elastic membrane, Int. J. Numer. Meth. Biomed. Eng. 30 (2014) 726–754, doi:10.1002/cnm.2624.
[22] H. Ding, P.D.M. Spelt, Wetting condition in diffuse interface simulations of contact line motion, Phys. Rev. E 75 (2007) 046708, doi:10.1103/PhysRevE.75.046708.
[23] H.G. Lee, J. Kim, Accurate contact angle boundary conditions for the Cahn–Hilliard equations, Comput. Fluids 44 (2011) 178–186, doi:10.1016/j.compfluid.2010.12.031.
[24] A.L. Bertozzi, S. Esedoglu, A. Gillette, Inpainting of binary images using the Cahn–Hilliard equation, IEEE Trans. Image Process. 16 (1) (2007) 285–291, doi:10.1109/TIP.2006.887728.
[25] J. Kim, A continuous surface tension force formulation for diffuse-interface models, J. Comput. Phys. 204 (2005) 784–804, doi:10.1016/j.jcp.2004.10.032.
[26] Y. Li, A. Yun, D. Lee, J. Shin, D. Jeong, J.S. Kim, Three-dimensional volume-conserving immersed boundary model for two-phase fluid flows, Comput. Methods Appl. Mech. Eng. 257 (2013) 36–46, doi:10.1016/j.cma.2013.01.009.